On-Chip Optical Isolator Based on Periodically Poled Lithium Niobate

Najiao Zhang(张娜娇)[1,2,†], Yijie Xia(夏逸杰)[1,2,†], Xiyao Song(宋锡耀)[1,2], Ya Jin(金亚)[1,2], Huashun Wen(文花顺)[1,2,3], Kunpeng Zhai(翟鲲鹏)[1,2], Xiaowei Wang(王晓伟)[4], Sha Zhu(朱厦)[1,2,3,*], Ninghua Zhu(祝宁华)[1,2,3]

[1]*Institute of Intelligent Photonics, Nankai University, Tianjin 300071, China*
[2]*National Key Laboratory of Semiconductor Laser, Nankai University, Tianjin 300071, China*
[3]*Academy for Advanced Interdisciplinary Studies, Nankai University, Tianjin 300071, China*
[4]*School of Instrumentation and Optoelectronic Engineering, Beihang University, Beijing 100191, China*

Chip-scale optical communication and integrated photonic systems require stable unidirectional light propagation, making the monolithic integration of optical isolators essential. We show a passive, non-magnetic optical isolator based on a periodically poled lithium niobate (PPLN) waveguide that utilizes the difference-frequency generation (DFG) effect to achieve nonreciprocal light transmission. By integrating interleavers, a narrow waveguide, and an asymmetric directional coupler (ADC) on the same thin-film lithium niobate (TFLN) chip, the device achieves nonreciprocal transmission through efficient forward DFG and engineered filtering, enabling strong suppression of backward-propagating signals. Benefiting from these mechanisms, the isolator achieves a simulated isolation ratio exceeding 40 dB at several wavelengths. The proposed structure combines nonlinear frequency conversion and wavelength-selective routing on the same TFLN platform without magnetic materials or continuous electrical modulation.

Keywords: Nonlinear optics (42.65.-k), Optical frequency converters (42.79.Nv), Integrated optics (42.82.-m), Optical waveguides and couplers (42.79.Gn).

1. Introduction

Optical isolators are indispensable components in modern photonic systems, serving to prevent unwanted back reflections and feedback that can destabilize lasers or interfere with signal transmission. They are essential in applications such as optical communication [1, 2], laser stabilization [3], radar detection [4], and integrated photonic signal processing [5], where unidirectional light propagation ensures system stability and performance.

Conventional optical isolators are primarily based on magneto-optic effects, with representative implementations based on Faraday rotation in magneto-optic materials [6-9]. Although these devices exhibit excellent isolation performance, they typically rely on bulky magnetic materials and external magnetic fields, making monolithic integration with mainstream photonic platforms such as silicon or lithium niobate difficult. To overcome these limitations, non-magnetic integrated isolators have

† These authors contributed equally to this work.
* Corresponding author. E-mail: zhusha@nankai.edu.cn

attracted growing attention in recent years [10-12]. Accordingly, a broad range of non-magnetic isolation schemes, which are generally categorized into active and passive approaches, have been proposed and demonstrated for on-chip nonreciprocal transmission. However, their intrinsic limitations continue to constrain practical deployment in large-scale, system-level photonic integration. Active isolators typically employ spatiotemporal modulation, such as electro-optic [13] or thermo-optic [14] modulation, to introduce time-varying coupling and thereby break Lorentz reciprocity for nonreciprocal transport. Recent demonstrations of traveling-wave electro-optic isolators on thin-film lithium niobate (TFLN) platforms achieve high isolation ratios with low insertion loss and relatively broad operating bandwidths by precisely matching the velocities of microwave and optical waves, such that forward-propagating light remains largely unmodulated while backward-propagating light is efficiently converted into frequency sidebands [15]. However, these electro-optic isolators still rely on continuous radio-frequency driving and careful microwave–optical co-design, typically requiring substantial RF power and precise phase control, which introduce additional circuit complexity and power consumption and pose challenges for energy efficiency, packaging, and long-term stability at the system level.

In contrast to actively modulated schemes, passive non-magnetic isolators do not require continuous electrical or thermal driving and therefore can eliminate static electrical/thermal tuning power, reduce system complexity, and improve operational stability. Such devices typically rely on optical nonlinearities or direction-dependent energy conversion processes to achieve nonreciprocal transmission, with representative examples including $\chi^{(3)}$-based isolators exploiting the Kerr effect [16, 17] or four-wave mixing [18, 19]. Related $\chi^{(3)}$-based schemes have also combined cavity-enhanced four-wave mixing with wavelength-selective routing to realize direction-dependent transmission [20]. Although this concept is similar to the present use of nonlinear frequency conversion and spectral routing, these schemes rely on $\chi^{(3)}$ FWM and cavity resonance. In a recent Kerr-nonlinearity-based optical isolator [21], backward-propagating light is suppressed through asymmetric nonlinear phase accumulation or resonance frequency shifts experienced by forward and backward propagation, and passive, non-magnetic on-chip nonreciprocal behavior has been demonstrated across multiple integrated photonic platforms. However, owing to the intrinsically weak $\chi^{(3)}$ nonlinearity, such approaches typically require trade-offs among pump power, interaction-enhancement schemes, and device scale. High pump power, long interaction lengths, or resonant enhancement impose system-level constraints in terms of energy consumption, footprint, bandwidth, and operational stability, thereby limiting their scalability for integrated photonic applications.

At the system level, TFLN has emerged as a highly competitive integrated photonic platform, enabled by its large electro-optic coefficient, broadband electro-optic response, and compatibility with mature nanofabrication processes [22]. These attributes have supported electro-optic modulators with bandwidths exceeding 100 GHz [23], reconfigurable filters [24], and various nonlinear devices, establishing TFLN as a core platform for chip-scale optical communication [25], microwave

photonics [26], and high-speed signal processing. From a system-integration perspective, however, achieving stable unidirectional light flow on the TFLN platform remains a nontrivial challenge. Architectures that rely on continuous external driving and carefully engineered spatiotemporal modulation introduce additional system complexity and hinder seamless co-integration with passive functional components, particularly in densely integrated photonic circuits. This limitation is especially restrictive for such integrated photonic systems, including TFLN-based laser-integrated transmitters and coherent photonic architectures, where even weak back reflections can degrade modulation fidelity and overall system performance. Accordingly, there is a strong motivation to realize a passive, non-magnetic optical isolator that can be monolithically integrated within the TFLN platform. A passive isolation mechanism that operates without continuous external modulation fundamentally differs from actively driven schemes at the system level, offering a more natural pathway toward robust unidirectional transmission.

In this work, we propose and numerically demonstrate a passive, non-magnetic optical isolator monolithically integrated on the TFLN platform. The isolator is based on a periodically poled lithium niobate (PPLN) waveguide that exploits the difference-frequency generation (DFG) process to enable nonreciprocal light transmission without continuous external modulation. By co-integrating interleavers, a narrow waveguide and an asymmetric directional coupler (ADC) within the same TFLN platform, the proposed device simultaneously achieves wavelength-selective routing and directional discrimination between forward and backward propagation. The nonreciprocal behavior arises from efficient forward DFG combined with engineered filtering operation, leading to strong suppression of backward-propagating signals. As a result, the proposed isolator exhibits a simulated isolation ratio exceeding 40 dB at several wavelengths. By avoiding continuous electrical or thermal modulation and remaining compatible with monolithic TFLN integration, the proposed approach provides a system-compatible pathway toward optical isolation, while naturally supporting seamless co-integration with high-speed modulators, filters, and nonlinear functional devices on the TFLN platform.

2. Method and Principle

The proposed optical isolator is designed based on breaking the reciprocity of light propagation in a waveguide [27]. As illustrated in Fig. 1, the device consists of one pair of interleavers, a narrow waveguide, an asymmetric directional coupler (ADC), and a periodically poled lithium niobate (PPLN) waveguide, with the detailed design parameters of these components provided in Section 3. In the schematic, the spectral information of the forward-propagating light is illustrated by the spectral evolutions labeled (I) to (IV) in the upper region, whereas that of the backward-propagating light is represented by the corresponding evolutions marked (IV) to (I) in the lower region. To make the wavelength routing more explicit, the propagation paths are marked directly on the device schematic, with black arrows indicating the forward routes and red arrows indicating the corresponding backward routes through the interleavers and ADC. In these spectral evolution diagrams, the red dashed lines denote the filtering effect of the corresponding components. The optical

isolation is primarily achieved through the combined action of the interleavers, which serve as wavelength-selective filters, and the DFG process in the PPLN waveguide.

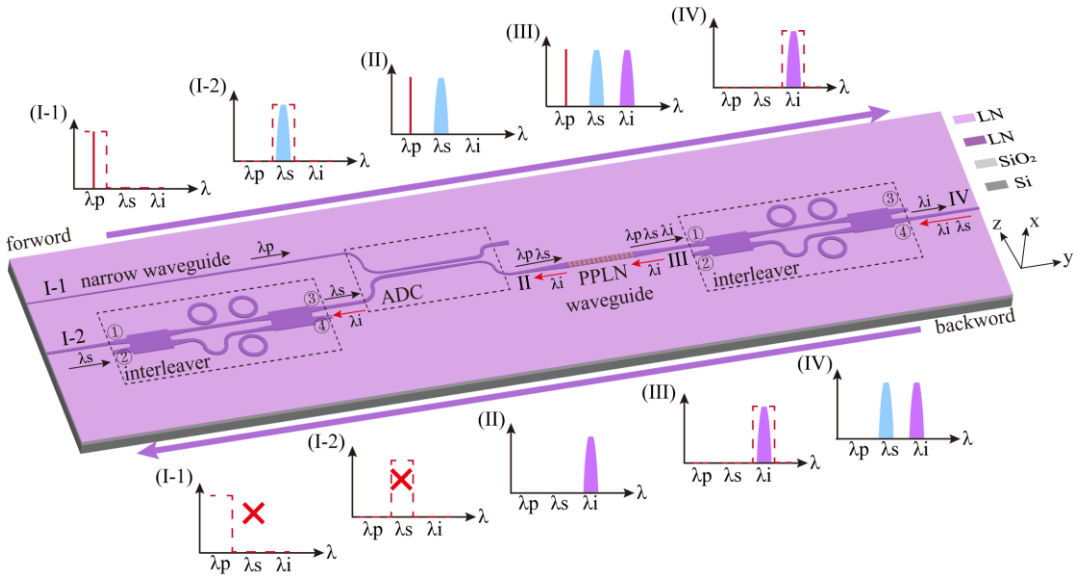


Fig. 1. The structure and workflow of the optical isolator. ADC: asymmetric directional coupler, PPLN: periodically poled lithium niobate

In the forward direction, the signal light couples into the input waveguide and propagates through port 3 of the input-side interleaver, which is designed to exhibit high transmittance at the signal light λ_s (~ 1510 nm). Meanwhile, the pump light at λ_p = 765 nm is coupled into the device via a narrow waveguide, combined with the signal light by a 1:1 ADC and launched into the PPLN section. The narrow waveguide is designed to support only the propagation of the pump light at λ_p = 765 nm. Within the PPLN waveguide, the pump light λ_p and signal light λ_s mix to generate an idler light ($\lambda_i = (\lambda_p^{-1} - \lambda_s^{-1})^{-1}$) through the DFG process. The forward-propagating waves then pass through the output-side interleaver. The signal light is transmitted through port 3, while the idler light at λ_i (~1550 nm) is routed to port 4. The ports exhibit low transmittance for the pump light, completing the wavelength routing required for forward transmission.

In contrast, when the signal light enters from the backward direction, it is routed by the output-side interleaver to port 2 rather than being coupled into the isolator section. For the idler light, it is transmitted through port 1 of the output-side interleaver into the PPLN section and then propagates toward the input port via the ADC. However, it can neither propagate through the narrow waveguide designed for the pump light nor be routed to port 1 of the input-side interleaver, since the idler wavelength is directed to port 2 of the input-side interleaver. As a result, the idler light cannot reach the input port of the isolator. It should also be noted that the backward-propagating signal and idler lights do not engage in nonlinear interactions with the forward-propagating pump due to a significant wavevector mismatch. The PPLN period is designed for quasi-phase matching (QPM) of the co-propagating pump, signal, and idler waves. When the signal or idler reverses direction while the pump remains forward-propagating, its wave vector changes sign, whereas the grating vector of the poled structure remains unchanged. The momentum compensation

required for forward DFG is lost. The nonlinear fields generated along the waveguide no longer accumulate coherently, resulting in negligible backward DFG. Therefore, the proposed device provides nonreciprocal transmission and achieves optical isolation.

The isolation performance of the device can be quantitatively evaluated by comparing the forward and backward transmission powers. Forward transmission is enabled by the efficient conversion of the signal light to the idler light via the DFG process in the PPLN, whereas backward propagation is subjected to strong suppression by the interleaver. Consequently, only a small fraction of backward-propagating signal light can reach the input port, yielding a large nonreciprocal transmission contrast. The isolation ratio (ISO) of the device is thus defined as [28]:

$$\mathrm{ISO}(\mathrm{dB}) = 10\log_{10}\left(\frac{P_{\mathrm{i_fwd}}}{P_{\mathrm{s_bwd}}}\right), \tag{1}$$

where $P_{\mathrm{i_fwd}}$ and $P_{\mathrm{s_bwd}}$ denote the forward idler power and backward signal power, respectively, which incorporate the nonlinear conversion efficiency of the PPLN and the wavelength-selective response of the interleaver.

3. Results and Discussion

3.1. The structure and performance of the designed PPLN waveguide

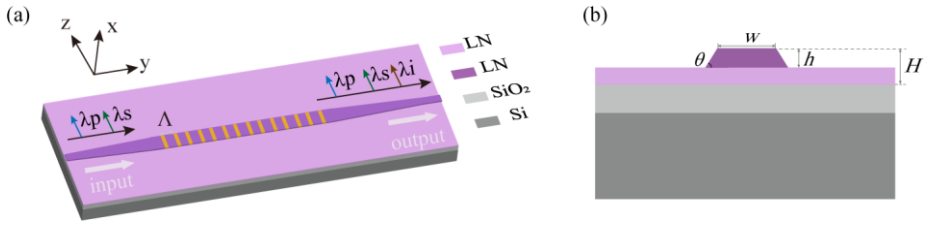


Fig. 2. Structure of the periodically poled lithium niobate (PPLN) waveguide. (a) 3D view; (b) cross-sectional view.

The functionality of the proposed isolator relies on the frequency conversion from the signal light to the idler light, which is facilitated by a PPLN waveguide. Fig. 2 illustrates its structure, where Fig. 2(a) presents the 3D view and Fig. 2(b) shows the waveguide cross-section. Specifically, Λ is the poling period, w denotes the top width of the waveguide, H and h represent the thickness of the LN thin film and the etch depth, respectively, while θ denotes the etch angle. As can be seen from Fig. 2(a), the DFG process is initiated by the interaction of the pump light λ_{p} and signal light λ_{s} through the second-order nonlinear susceptibility, generating an idler light λ_{i}. The evolution of the optical field amplitudes for the pump A_{p}, signal A_{s}, and idler A_{i}, which are expressed in units of $\mathrm{W}^{1/2}$, along the propagation direction y is governed by the following coupled-wave equations [29]

$$\begin{cases} \dfrac{dA_s}{dy} = -i\kappa_s A_i^* A_p e^{-i\Delta ky} \\ \dfrac{dA_i}{dy} = -i\kappa_i A_s^* A_p e^{-i\Delta ky} \\ \dfrac{dA_p}{dy} = -i\kappa_p A_s A_i e^{i\Delta ky} \end{cases}. \tag{2}$$

Here, Δk represents the phase mismatch, defined as

$$\Delta k = k_p - k_s - k_i - \frac{2\pi}{\Lambda}, \tag{3}$$

where k_j (j = p, s, i) represent the wave vectors of the pump, signal, and idler lights, respectively, and Λ is the poling period of the PPLN. For efficient conversion, the QPM condition must be met ($\Delta k = 0$).

The nonlinear coupling coefficient κ_j in Eq. (2) is given by:

$$\kappa_j = \omega_j \cdot \sqrt{\frac{2\mu_0 d_{eff}^2}{n_p n_s n_i c A_{eff}}}, \tag{4}$$

where ω_j and n_j are the angular frequency and effective refractive index of the respective interacting wave, d_{eff} is the effective second-order nonlinear coefficient (approximately 17.2 pm/V in X-cut PPLN waveguides), and A_{eff} denotes the effective mode overlap area.

To evaluate the performance of PPLN-based nonlinear waveguides, the normalized nonlinear conversion efficiency η is widely used as a key figure of merit and serves as a critical basis for device optimization. For DFG, η is related to the idler nonlinear coupling coefficient κ_i and the interaction length L as:

$$\eta = \kappa_i^2 \cdot \mathrm{sinc}^2\left(\frac{\Delta kL}{2}\right), \tag{5}$$

Another crucial parameter affecting broadband performance is the group velocity mismatch (GVM) between the signal and idler lights, defined as:

$$\mathrm{GVM} = v_{g,i}^{-1} - v_{g,s}^{-1}, \tag{6}$$

where $v_{g,i/s}$ are the group velocities of the idler λ_i and signal λ_s. For the PPLN waveguide, broadband phase matching is optimized when the GVM approaches zero, leading to an increased operational bandwidth and a correspondingly flatter wavelength-dependent response of the nonlinear conversion efficiency [30].

The waveguide's geometrical parameters primarily govern both η and GVM. The proposed optical isolator is designed on a TFLN wafer with a thickness of H = 500 nm and an etch depth h = 250 nm. Under the operating conditions of a 765 nm pump light and a signal light centered at 1510 nm, the subsequent optimization of both η and GVM is performed by varying the waveguide width, as shown in Fig. 3.

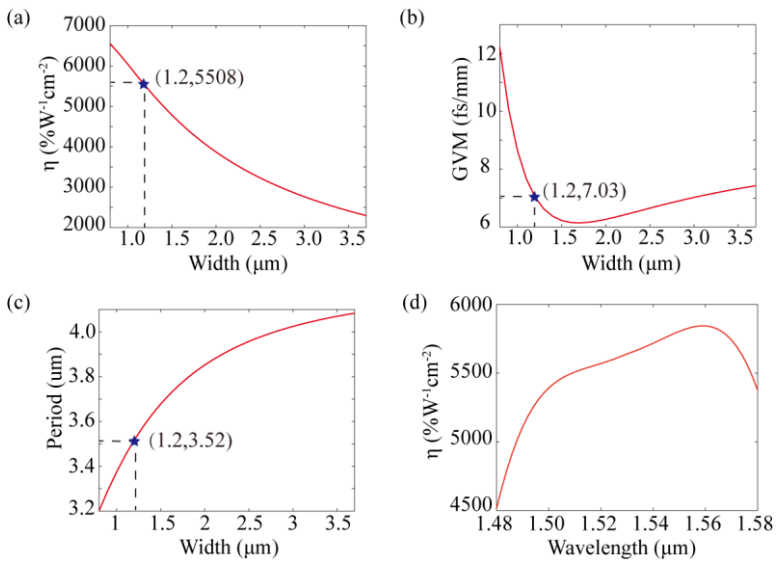


Fig. 3. (a) Normalized conversion efficiency η, (b) group velocity mismatch (GVM), and (c) poling period of the PPLN waveguide as a function of the waveguide width. (d) η of the designed PPLN waveguide as the signal wavelength varies from 1480 nm to 1580 nm.

Fig. 3(a) reveals a monotonic decrease in the normalized conversion efficiency η over the waveguide width range of 0.8 to 3.7 μm. This reduction arises primarily from the gradual weakening of modal confinement and field overlap between the interacting waves in wider waveguides, which leads to a lower effective nonlinear coupling strength. Fig. 3(b) presents the variation of the GVM with the waveguide width. A large GVM is undesirable as it reduces the DFG bandwidth; it is therefore crucial to minimize it. Fig. 3(c) shows the poling period of the PPLN waveguide as a function of the waveguide width. As the waveguide width increases, the effective refractive indices of the interacting modes vary due to changes in optical confinement, thereby modifying the phase-matching condition. To satisfy the QPM requirement for efficient DFG, the corresponding poling period must be adjusted accordingly.

By jointly analyzing the results in Fig. 3(a) and 3(b), a waveguide width of 1.2 μm is identified as the optimal design point, offering a balanced trade-off between minimizing GVM and maintaining sufficient nonlinear coupling efficiency. For the selected 1.2 μm-wide waveguide, the calculated poling period is 3.52 μm, which ensures precise phase matching and efficient DFG operation. Fig. 3(d) shows its normalized conversion efficiency η as the signal wavelength varies from 1480 nm to 1580 nm. A 3-cm interaction length is adopted in the numerical model to provide sufficient nonlinear conversion. This length remains within the centimeter-scale regime demonstrated for TFLN PPLN waveguides [31], although the longer interaction length places tighter requirements on structural uniformity and propagation loss. The designed PPLN waveguide exhibits high conversion efficiency across the operational bandwidth of the isolator, thereby providing a solid foundation for high-performance DFG-based optical isolation.

3.2. The structure and performance of the narrow waveguide, couplers and filters

Following the description of the overall architecture and operating principle of the optical isolator, this section examines the performance of the key components other than the PPLN nonlinear waveguide. The device comprises a narrow waveguide, an asymmetric directional coupler (ADC), and a pair of interleaver filters, which serve to realize pump transmission, wavelength-selective coupling, and the separation and routing of different wavelength bands, respectively. The loss, coupling characteristics, spectral response, and port selectivity of these components collectively govern the propagation of each wavelength channel within the device and thus the overall isolation performance of the cascaded system.

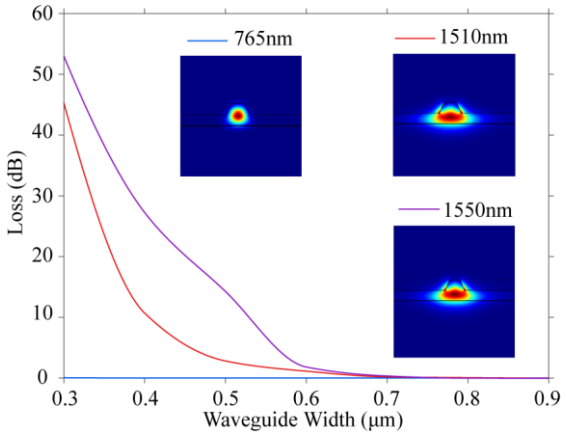


Fig. 4. Propagation loss and mode profiles of the narrow waveguide.

The narrow waveguide section adopts a reduced width to suppress the transmission of backward-propagating signal and idler light. Fig. 4 presents the transmission loss of the fundamental TE mode at pump, signal, and idler wavelengths as a function of waveguide width for a 4-mm-long narrow waveguide. The insets show the corresponding optical field distributions at a waveguide width of 0.3 μm. As shown in Fig. 4, the pump light maintains low loss across the entire waveguide width range, indicating effective mode confinement and stable propagation. By contrast, the loss at the signal light increases sharply in narrow waveguides. The field profiles further confirm that, at a waveguide width of 0.3 μm, the mode of signal light is no longer well confined as the fundamental TE mode, resulting in significant leakage from the waveguide and the loss of guided propagation. A similar trend is observed for the idler light at approximately 1550 nm. While a narrower waveguide would improve the suppression of backward signal and idler light, 0.3 μm is chosen as a practical trade-off between performance and fabrication difficulty. The narrow waveguide therefore allows efficient transmission of the pump light while strongly suppressing the signal and idler light, which satisfies the design target of the pump channel. In short, the narrow waveguide realizes a pump-only passband and provides high rejection for both signal and idler light.

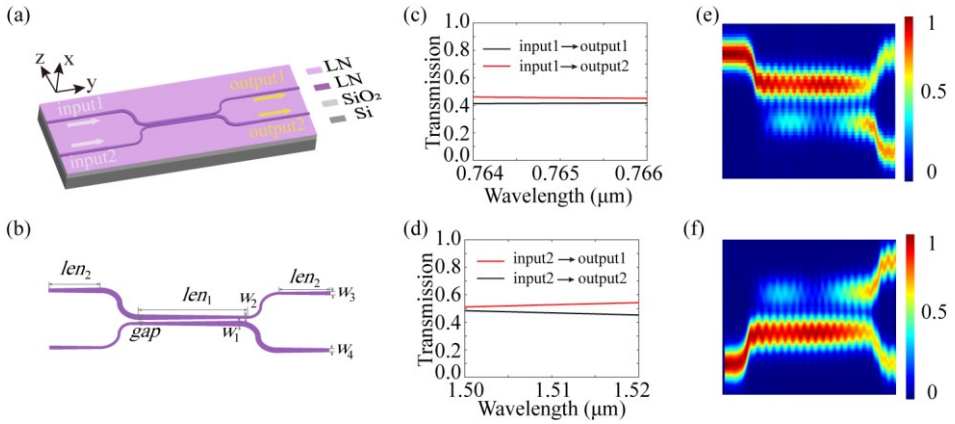


Fig. 5. The structure and transmission of the ADC at signal λ_s and pump λ_p. (a) 3D view. (b) Top view. (c) and (d) The transmission of pump λ_p. (e) and (f) The transmission of signal λ_s.

To couple the pump and signal into the PPLN waveguide, a compact ADC with tapered input and output sections was designed and integrated on the same TFLN platform. The structural layout and field evolution of the ADC are shown in Fig. 5. As shown in Fig. 5(a) and 5(b), the coupler consists of two symmetrically arranged lithium niobate waveguides whose widths gradually vary along the propagation direction. The two tapered waveguides with w_1 = 1.68 μm and w_2 = 1.38 μm are mirror-symmetric about the y-axis, forming an adiabatic coupling region with a designed coupling length len_1 = 203 μm and gap gap = 0.44 μm, which enables controllable evanescent coupling between the guided modes. The tapered input and output waveguides have widths of w_3 = 1.53 μm and w_4 = 1.78 μm, respectively. In the isolator configuration, the pump and signal light are launched into input 1 and input 2, respectively. The combined waves are then collected at output 2 and coupled into the PPLN waveguide. Fig. 5(c) and 5(d) present the simulated power transfer characteristics at the operating wavelengths, where the optical power of the two output ports exhibits complementary behavior. The black and red curves in the figures correspond to the transmission responses obtained when light is launched from different input ports and collected at the respective output ports. At the design wavelengths (λ_s ~ 1510 nm and λ_p = 765 nm), approximately 1:1 power splitting is achieved, confirming that the ADC functions as a balanced 3 dB coupler. The 1:1 splitting ratio defines the designed operating condition of the ADC. Deviations from this ratio change the pump and signal powers coupled into the PPLN waveguide, affecting the generated idler power and the resulting isolation ratio. Maintaining the coupling ratio close to the designed value is therefore important for achieving the predicted isolation performance. By combining adiabatic waveguide shaping and tapered transitions, the ADC provides broadband operation and reliable mode matching between the filtering stage and the nonlinear PPLN conversion region.

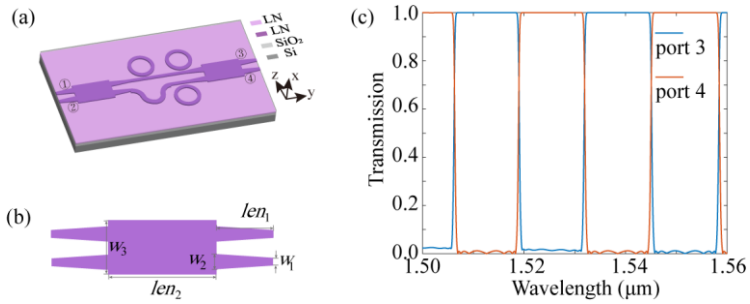


Fig. 6. The structure and transmission of the interleaver at signal λ_s and idler λ_i. (a) 3D view. (b) Top view of the Multimode Interference (MMI). (c) The transmission at ports 3 and 4 of the interleaver.

As shown in Fig. 6(a), the interleaver consists of an unequal-arm Mach–Zehnder interferometer (MZI) cascaded with three microring resonators. The unequal-arm MZI is formed by two 2×2 MMIs with a 1:1 power splitting ratio, and the key dimensions of the MMI section are given in Fig. 6(b), including len_1 = 10.06 μm, len_2 = 85.88μm, w_1 = 1 μm, w_2 = 2.6 μm, and w_3 = 9.7 μm. The unequal path length in the MZI provides the basic periodic interference response for wavelength interleaving, while the three microrings are used to further shape the spectrum. The rings share the same round-trip delay $T_r = 6 \times 10^{-13}$ and phase condition $\phi = \pi$, giving the same resonance period, whereas their coupling coefficients are 0.96, 0.68, and 0.25, respectively. This design sharpens the spectral roll-off and improves stopband rejection. The MZI arm delay is set to $T_t = 3 \times 10^{-13}$ s, matching the MZI interference period to the ring resonance response and enabling complementary wavelength routing at the two output ports.

Figure 6(c) shows the transmission spectra of port 3 and port 4. In the 1507–1518 nm range, port 3 exhibits high transmission while port 4 is suppressed, indicating that the signal band centered near 1510 nm is routed to port 3. In the 1547–1557 nm range, the response is reversed, with the idler band centered near 1550 nm routed to port 4. The two ports therefore show clear complementary responses over the wavelength range of interest, enabling wavelength separation of the signal and idler in the integrated DFG isolator. Each wavelength-routing window spans approximately 10 nm, providing the required spectral separation between the signal and idler channels.

3.3. Performance of the isolator

The signal wavelength-dependent isolation ratio of the proposed optical isolator is presented in Fig. 7. The device achieves this performance with a pump power of 10 mW and a signal input power of 0.5 mW. Under these conditions, the isolation spectrum exhibits multiple sharp peaks exceeding 40 dB, while the broad isolation remains above 28 dB over an 8-nm signal-wavelength range from 1507 to 1515 nm.

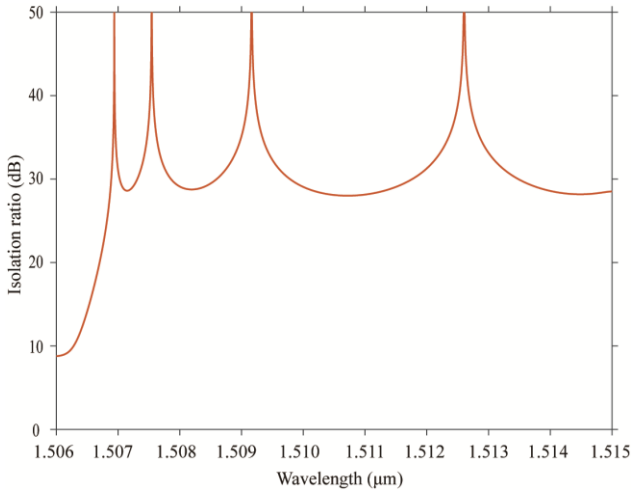


Fig. 7. Wavelength-dependent isolation ratio of the proposed optical isolator under a pump power of 10 mW and a signal input power of 0.5 mW.

These observed isolation characteristics can be well interpreted in conjunction with the spectral response of the interleaver filters. Specifically, sharp isolation peaks exceeding 40 dB appear at signal wavelengths of 1507 nm, 1507.6 nm, 1509.2 nm, and 1512.7 nm, which correspond to the transmission minima of port 4 in the interleaver spectrum shown in Fig. 6(c). At these dips, the interleaver provides strong suppression of the signal light, giving rise to the high-isolation spikes. Meanwhile, the roll-off of the isolation ratio near 1506 nm and 1516 nm is consistent with the filtering response of the interleavers. Moreover, the broadband isolation level can be increased by increasing the pump power, which strengthens the signal-to-idler conversion process.

In addition to the isolation ratio, we estimated the on-chip forward-path insertion loss of the device. Here, the insertion loss refers to the linear transmission loss along the designated forward optical path. The insertion-loss estimate in the PPLN waveguide considers the linear propagation loss. With the current fabrication process in our group, the propagation losses of conventional TFLN single-mode waveguides and PPLN waveguides are 0.4 dB/cm and 1 dB/cm, respectively. The insertion loss of the 3-cm PPLN waveguide used in this work is approximately 3 dB. For the interleavers, the calculation includes the FDTD-derived MMI power transmission and the propagation losses of the MZI waveguides and microrings. At the signal and idler operating wavelengths, the simulated insertion losses of the two interleavers are approximately 0.75 dB and 0.21 dB. The simulated transmittance at the designated ADC output port at 1510 nm is approximately 0.477, corresponding to a forward-path loss of about 3.22 dB. The total additional connecting-waveguide length is approximately 500 μm based on our layout experience. Its propagation loss is about 0.02 dB and is negligible compared with the losses of the main functional components. The narrow waveguide lies in the pump branch and is not included in the signal-path insertion-loss estimate. Therefore, the total on-chip forward-path insertion loss is estimated to be approximately 7.20 dB.

Table 1 presents a comparative analysis of the isolator performance proposed in this work against that of TFLN-based isolators reported in the literature, with respect

to various implementation approaches. It can be observed that the proposed isolator achieves a relatively high theoretical isolation ratio. Among the devices listed in Table 1, the proposed device provides a theoretical isolation ratio above 40 dB with an estimated forward-path insertion loss of approximately 7.2 dB. The 8-nm operating bandwidth is narrower than that of several previously reported broadband schemes.

Table 1. Performance comparison of integrated TFLN isolators

Ref	Method	Active/ Passive	Insertion loss (dB)	Isolation (dB)	Bandwidth	Exp./ Theo.
[28]	Three-wave mixing	Passive	~14	18	>150 nm	Exp.
[32]	acousto-optic polarization rotation	Active	—	21	>150 GHz	Exp.
[33]	EO modulation	Active	~10	27	—	Exp.
[34]	EO modulation	Active	<0.5	15	~100 nm	Exp.
[35]	Magneto-optic effect	—	2.736	30	>48.3 nm	Theo.
This work	Three-wave mixing	Passive	~7.2	>40 (peak)	8 nm (1507–1515 nm, ＞28 dB broadband isolation)	Theo.

3.4. Fabrication Feasibility and Tolerance Analysis

The proposed device combines a centimeter-scale PPLN waveguide, two interleavers, a narrow waveguide, and an ADC on the same TFLN platform. The interleavers, narrow waveguide, ADC, and connecting waveguides are passive TFLN structures that can be fabricated using conventional lithography and etching processes. The PPLN section requires an additional periodic-poling step, and centimeter-scale PPLN waveguides have also been experimentally demonstrated. Chen et al. used adapted poling to compensate for phase mismatch induced by local structural nonuniformity and maintained coherent nonlinear interaction over long propagation lengths [31]. The PPLN geometry and operating conditions in Ref. [31] differ from those considered here, but the demonstrated long periodically poled TFLN waveguides provide an experimental reference for the present design. These demonstrations support the fabrication feasibility of the proposed integrated structure.

Fabrication tolerance is evaluated using representative parameters for each component. The narrow waveguide is examined using its width-dependent propagation loss. The PPLN section is analyzed by varying the waveguide width, etch depth, and TFLN film thickness. The interleaver tolerance is represented by an equivalent spectral shift. The ADC is evaluated by varying the waveguide width and

coupling gap. The corresponding effects on wavelength routing, nonlinear conversion, and isolation performance are discussed below.

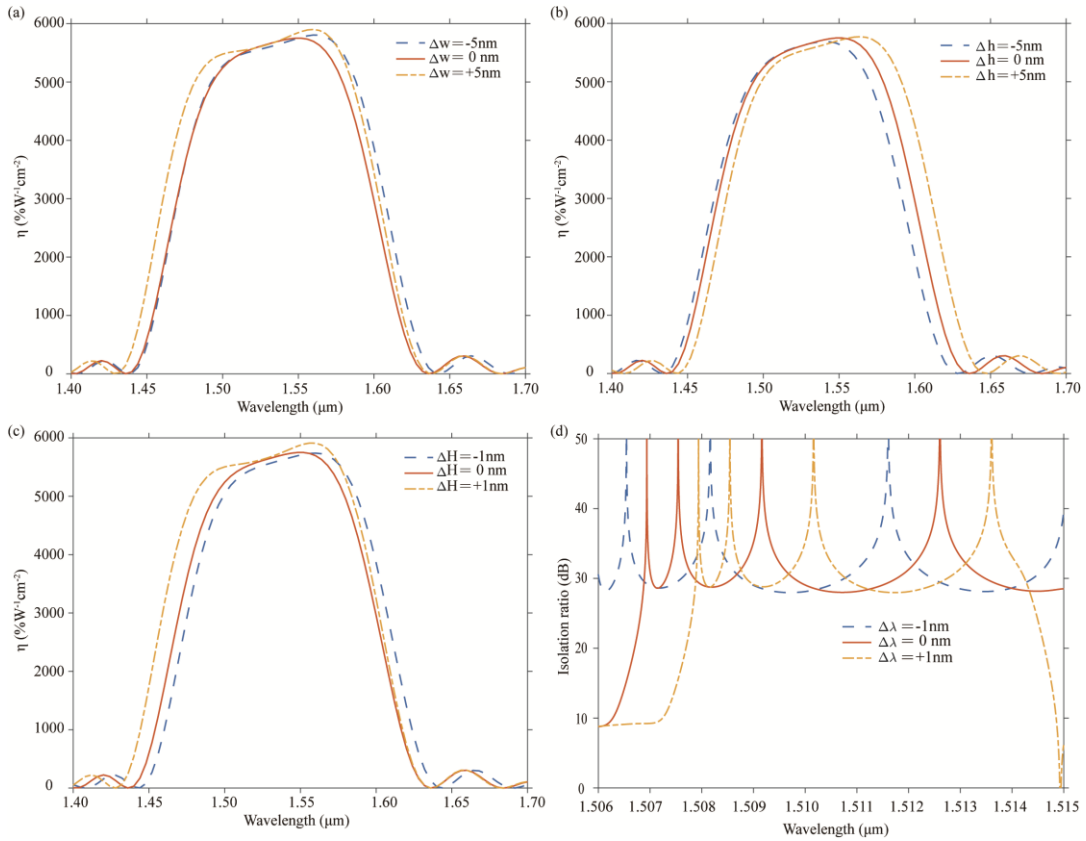


Fig. 8. Fabrication tolerance analysis. PPLN normalized conversion efficiency under variations in (a) waveguide width, (b) etch depth, and (c) TFLN film thickness. (d) Isolation ratio under interleaver spectral shifts.

The width tolerance of the narrow waveguide was evaluated using the propagation-loss results in Fig. 4. The loss at 765 nm remains close to 0 dB over the 0.3–0.4 μm width range. The signal and idler remain strongly attenuated throughout this range. The wavelength-selective function is preserved over a 100 nm waveguide-width range, indicating a large fabrication tolerance for the narrow waveguide.

For the PPLN section, the waveguide width w, etch depth h, and TFLN film thickness H were different from the nominal values. The waveguide width and etch depth were changed by ±5 nm, while the TFLN film thickness was varied by ±1 nm. Fig. 8(a)–8(c) show that these variations move the QPM window with little change in the spectral shape or peak normalized conversion efficiency. The resulting DFG conversion window still overlaps the interleaver operating band. The overall isolation performance is expected to remain stable.

The interleaver tolerance was evaluated by applying equivalent wavelength shifts of ±1 nm to the nominal transmission spectra. Figure 8(d) shows the corresponding isolation ratio. The nominal structure provides an isolation ratio above 28 dB across 1507–1515 nm. A −1 nm shift maintains an isolation ratio above 25 dB over 1506–1515 nm, giving a 9.0 nm continuous bandwidth. A +1 nm shift provides a 6.7 nm

bandwidth above 25 dB over 1507.8–1514.5 nm. The device maintains effective isolation over several nanometers under the considered spectral shifts.

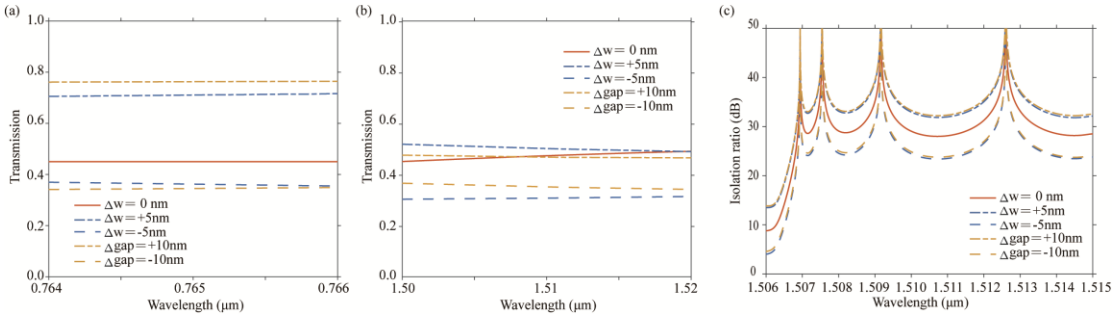


Fig. 9. Fabrication-tolerance analysis of the ADC. (a) Pump transmittance at 765 nm, (b) signal transmittance over 1500–1520 nm, and (c) isolation spectra under waveguide-width and coupling-gap variations.

For the ADC, we considered waveguide-width offsets of ±5 nm and coupling-gap offsets of ±10 nm. Fig. 9(a)–(b) show the target-port transmittance of the pump and signal. At 765 nm, the nominal ADC gives a pump transmittance of about 0.45, which varies between 0.35 and 0.76 after introducing the width and gap offsets. Near 1510 nm, the signal transmittance spans approximately 0.31–0.50 under the same offsets, compared with about 0.48 for the nominal ADC. Structural variations alter the pump and signal powers delivered to the PPLN waveguide. The corresponding variation in isolation is much smaller, as shown in Fig. 9(c). The spectral trend and high-isolation peak positions remain similar, while the isolation ratio stays above 20 dB over 1507–1515 nm. Broadband isolation is preserved within the examined ADC fabrication range.

Temperature also affects the device performance through the thermo-optic effect. The resulting refractive-index variation modifies the QPM condition and the spectral position of the PPLN conversion band. Previous experiments have demonstrated controllable thermal tuning and realignment of the QPM spectrum, enabling recovery of the nonlinear conversion efficiency [36]. In practical operation, a thermoelectric cooler (TEC) can stabilize the chip temperature and preserve both the QPM condition and the spectral overlap between the PPLN conversion band and the interleaver response.

4. Conclusion

In conclusion, we have proposed and numerically demonstrated a passive, non-magnetic optical isolator monolithically integrated on the TFLN platform. By exploiting DFG in a PPLN waveguide, the device achieves nonreciprocal light transmission without relying on continuous external modulation or magnetic materials. The co-integration of interleavers, an ADC, and a narrow waveguide enables wavelength-selective routing and effective discrimination between forward and backward propagation within a TFLN-compatible architecture. The proposed isolator leverages efficient forward DFG together with wavelength-selective filtering to strongly suppress backward-propagating signals, resulting in a simulated isolation ratio exceeding 40 dB at several wavelengths. By avoiding continuous electrical or thermal modulation while remaining compatible with monolithic TFLN integration,

this approach provides a system-compatible route toward optical isolation that naturally aligns with large-scale integration and co-integration alongside filters and nonlinear functional devices.

Acknowledgment

This work was supported in part by the National Key R&D Program of China (No. 2024YFB2808300), the National Natural Science Foundation of China (No. 62305008), the Fundamental Research Funds for the Central Universities (No. 063-63263242), the Fundamental and Interdisciplinary Disciplines Breakthrough Plan of the Ministry of Education of China (JYB2025XDXM121), and the Fund of State Key Laboratory of Photonics and Communications, P. R. China.

References

[1] Wang Y, Xu B, Zhang D, Xu S, Dong Z, Zeng X, Lu X and Pei J 2019 *Crystals* **9** 570

[2] Bekkali A, Fujita H and Hattori M 2022 *J. Lightwave Technol.* **40** 1509-1518

[3] Heim D A S, Bose D, Liu K, Isichenko A and Blumenthal D J 2025 *Nat. Commun.* **16** 5944

[4] Zhu S, Zhang Y, Feng J, Wang Y, Zhai K, Feng H, Pun E Y B, Zhu N H and Wang C 2025 *Nat. Photon.* **19** 204-211

[5] Zhang Y, Du Q, Wang C, Fakhrul T, Liu S, Deng L, Huang D, Pintus P, Bowers J, Ross C A, Hu J and Bi L 2019 *Optica* **6** 473-482

[6] Liu S, Minemura D and Shoji Y 2023 *Optica* **10** 1345-1352

[7] Yan W, Yang Y, Liu S, Zhang Y, Xia S, Kang T, Yang W, Qin J, Deng L and Bi L 2020 *Optica* **7** 1555-1562

[8] Meyer J G, Zablah A, Kapzems K, Kovalenko N and Pronin O 2024 *Opt. Express* **32** 29227-29238

[9] Zhang T T, Zhou W P, Li Z X, Tang Y T, Xu F, Wu H D, Zhang H, Tang J S, Ruan Y P and Xia K Y 2024 *Chin. Phys. Lett.* **41** 044205

[10] Nagulu A and Krishnaswamy H 2021 *IEEE J. Microw.* **1** 447-456

[11] Tian H, Liu J, Siddharth A, Wang R N, Blésin T, He J, Kippenberg T J and Bhave S A 2021 *Nat. Photon.* **15** 828-836

[12] Kittlaus E A, Jones W M, Rakich P T, Otterstrom N T, Muller R E and Rais-Zadeh M 2020 *Nat. Photon.* **15** 43-52

[13] Yu M, Reimer C, He L, Luke K, Puma E, Shao L, Shams-Ansari A, Grant H R, Johansson L, Zhang M and Lončar M 2022 *Conf. Lasers Electro-Optics* **1-2** STh1C.1

[14] Dostart N, Gevorgyan H, Onural D and Popovic M A 2021 *Opt. Lett.* **46** 460-463

[15] Yu M, Cheng R, Reimer C, He L, Luke K, Puma E, Shao L, Shams-Ansari A, Ren X, Grant H R, Johansson L, Zhang M and Lončar M 2023 *Nat. Photon.* **17** 666-671

[16] White A D, Ahn G H, Gasse K V, Yang K Y, Chang L, Bowers J E and Vučković J 2022 *Nat. Photon.* **17** 143-149

[17] Liu J C, Xia G Y, Hong Q L, Zhu P Y, Zhang K K, Xia K Y, Xu P, Qin S Q and Zhu Z H 2025 *Chin. Phys. B* **34** 034204

[18] Hua S, Wen J, Jiang X, Hua Q, Jiang L and Xiao M 2016 *Nat. Commun.* **7** 13657

[19] Carusotto I 2022 *arXiv* 2208.08350

[20] Zheng Y L, Yang J F, Shen Z H, Cao J J, Chen X F, Liang X G and Wan W J 2016 *Light Sci. Appl*. **5** e16072
[21] White A D, Ahn G H, Luhtaru R, Guo J, Morin T J, Saxena A, Chang L, Majumdar A, Van Gasse K, Bowers J E and Vučković J 2024 *Nat. Photon.* **18** 1305-1311
[22] Hu Y, Zhu D, Lu S, Zhu X, Song Y, Renaud D, Assumpcao D, Cheng R, Xin C J, Yeh M, Warner H, Guo X, Shams-Ansari A, Barton D, Sinclair N and Loncar M 2025 *Nat. Rev. Phys*. **7** 237-254
[23] Valdez F, Mere V and Mookherjea S 2023 *Optica* **10** 1056-1065
[24] Hou S, Chen P, Shah M, Briggs I, Xing W, Liu Z and Fan L 2023 *ACS Photonics* **10** 3896-3900
[25] Yu Z, Tong Y, Tsang H K and Sun X 2020 *Nat. Commun.* **11** 2602
[26] Feng H, Ge T, Guo X, Wang B, Zhang Y, Chen Z, Zhu S, Zhang K, Sun W, Huang C, Yuan Y and Wang C 2024 *Nature* **627** 80-87
[27] Yang S, Liu M, Zhao C, Fan S and Qiu C W 2024 *Nat. Photon.* **18** 412-424
[28] Abdelsalam K, Li T, Khurgin J B and Fathpour S 2020 *Optica* **7** 1304-1307
[29] Boyd R W, Gaeta A L and Giese E 2008 *Nonlinear optics 3rd edn* Springer
[30] Mishra J, Jankowski M, Hwang A Y, Stokowski H S, McKenna T P, Langrock C, Ng E, Heydari D, Mabuchi H, Safavi-Naeini A H and Fejer M M 2022 *Opt. Express* **30** 32752-32760
[31] Chen P K, Briggs I, Cui C, Zhang L, Shah M and Fan L 2024 *Nat. Nanotechnol.* **19** 44-50
[32] Shi H, Huang C, Zhang T, Zhang Y, Zheng T, Nie C, Liu C and Sun J 2026 *ACS Photonics* **13** 1075-1083
[33] Huang H, Balčytis A, Dubey A, Boes A, Nguyen T G, Ren G, Tan M and Mitchell A 2023 *Opto-Electron. Sci.* **2** 220022
[34] Shah M, Briggs I, Chen P K, Hou S and Fan L 2023 *Opt. Lett.* **48** 1978-1981
[35] Li M, Zhao Y, Dai S, Yu W, Li J, Lin T, Zhang Z and Liu J 2021 *Opt. Commun.* **495** 127088
[36] Li X, Li H, Wang Z, Chen Z, Ma F, Zhang K, Sun W and Wang C *2024 Photonics Res*. **12** 1703–1708